



# Blue-LED-excitable NIR-II luminescent lanthanide-doped SrS nanoprobe for ratiometric thermal sensing

Jiaojiao Wei<sup>1,2</sup>, Youyu Liu<sup>1,2</sup>, Meiran Zhang<sup>2</sup>, Wei Zheng<sup>1,2,3\*</sup>, Ping Huang<sup>1,2,3</sup>, Zhongliang Gong<sup>2</sup>, Renfu Li<sup>2,3</sup> and Xueyuan Chen<sup>1,2,3\*</sup>

**ABSTRACT** Lanthanide (Ln<sup>3+</sup>)-doped near infrared (NIR)-II luminescent nanoprobe have shown great promise in many technological fields, but are currently limited by the low absorption efficiency of Ln<sup>3+</sup> due to the forbidden 4f→4f transition. Herein, we report a novel NIR-II luminescent nanoprobe based on efficient energy transfer from Ce<sup>3+</sup> to Er<sup>3+</sup> and Nd<sup>3+</sup> in sub-10 nm SrS nanocrystals (NCs), which are excitable by using a commercial blue light-emitting diode (LED). Through sensitization by the allowed 4f→5d transition of Ce<sup>3+</sup>, the NCs exhibit strong NIR-II luminescence from Er<sup>3+</sup> and Nd<sup>3+</sup> with quantum yields of 2.9% and 2.3%, respectively. Furthermore, by utilizing the intense NIR-II luminescence of Er<sup>3+</sup> from the thermally coupled Stark sublevels of <sup>4</sup>I<sub>13/2</sub>, we demonstrate the application of SrS:Ce<sup>3+</sup>/Er<sup>3+</sup> NCs as blue-LED-excitable NIR-II luminescent nanoprobe for ratiometric thermal sensing. These findings reveal the unique advantages of SrS:Ln<sup>3+</sup> NCs in NIR-II luminescence, which may open up a new avenue for exploring novel and versatile luminescent nanoprobe based on Ln<sup>3+</sup>-doped sulphide NCs.

**Keywords:** SrS, lanthanide, near-infrared II, nanoprobe, thermal sensing

## INTRODUCTION

Lanthanide (Ln<sup>3+</sup>)-doped luminescent nanocrystals (NCs) emitting in the second near-infrared (NIR-II: 1000–1700 nm) biological window have recently evoked considerable interest, owing to their superior optical properties such as high photochemical stability, sharp emission peaks, long photoluminescence (PL) lifetimes, and large antenna-generated Stokes shift, in parallel with the benefits of minimal background interference and deep tissue penetration of the NIR light [1–9]. These outstanding features make Ln<sup>3+</sup>-doped NIR-II luminescent NCs ideal candidates as an alternative to traditional fluorescent probes like organic dyes and quantum dots and as a new generation of luminescent nanoprobe in many technological fields, including deep-tissue bioimaging, non-invasive chemical/biological detection, high-seed optical communication, and non-contact thermal sensing [10–22]. Nonetheless, because of the parity-forbidden nature of the 4f→4f electronic transitions, Ln<sup>3+</sup>-doped NIR-II luminescent NCs normally suffer from

low absorption and emission efficiencies, and exhibit low-to-medium brightness when compared with organic dyes and quantum dots [23–29]. Therefore, a high-power laser is generally demanded to realize bright NIR-II luminescence in Ln<sup>3+</sup>-doped NCs, which may limit their widespread applications.

To circumvent the limitation of Ln<sup>3+</sup>-doped NIR-II luminescent NCs, it is of fundamental importance to introduce an antenna that can effectively harvest the excitation light and sensitize the NIR-II luminescence of Ln<sup>3+</sup> emitters [30–33]. In this regard, optical entities of allowed transitions with large absorption cross-sections such as Ce<sup>3+</sup>, Bi<sup>3+</sup>, ligand-to-metal charge transfer states, and the host absorption of semiconductors can be effective sensitizers for Ln<sup>3+</sup> luminescence [34–37]. The absorption of these species, however, is influenced significantly by the host matrix with respect to the site symmetry, the crystal field (CF) strength, and the covalency [38–41]. Therefore, a judicious screening of host materials for both the sensitizers and Ln<sup>3+</sup> emitters is essential to the design of efficient NIR-II luminescent nanoprobe with desired properties.

Hitherto, most of the reported Ln<sup>3+</sup>-doped NIR-II luminescent nanoprobe have been restricted to fluorides, probably due to the well-established synthetic methods for their upconversion analogues [42–45]. Until recently, the new class of NIR-II luminescent nanoprobe based on Ln<sup>3+</sup>-doped sulphides (namely, CaS and NaGdS<sub>2</sub>) have been proposed by our group [46,47]. In comparison with fluorides, sulphide NCs exert a stronger CF and a higher covalency on Ln<sup>3+</sup> emitters [48–50]. As a result, the absorption and emission of Ce<sup>3+</sup> and Eu<sup>2+</sup> ions with allowed 4f→5d transitions locate at lower energies in sulphides (in the visible (vis) region) than in fluorides and oxides (in the ultraviolet (UV) region), which promises Ce<sup>3+</sup> and Eu<sup>2+</sup> activated sulphides as efficient phosphors in white light-emitting diodes (LEDs) [51–53]. Specifically, the absorption of Ce<sup>3+</sup> in alkaline-earth sulfides (e.g., CaS and SrS) in the blue region of the spectrum matches well with the emission of the commercial blue-LED chip. This enables the development of blue-LED-excitable NIR-II luminescent nanoprobe via energy transfer (ET) from Ce<sup>3+</sup> to NIR-II Ln<sup>3+</sup> emitters [46]. Moreover, owing to the strong CF level splitting, the luminescence of Ln<sup>3+</sup> via 4f→4f transitions in the sulphide system is characterized by sharp CF emission peaks even at room temperature (RT), which may facilitate the devise of smart thermal sensors based on NIR-II

<sup>1</sup> College of Chemistry, Fuzhou University, Fuzhou 350116, China

<sup>2</sup> CAS Key Laboratory of Design and Assembly of Functional Nanostructures, Fujian Key Laboratory of Nanomaterials, and State Key Laboratory of Structural Chemistry, Fujian Institute of Research on the Structure of Matter, Chinese Academy of Sciences, Fuzhou 350002, China

<sup>3</sup> Fujian Science & Technology Innovation Laboratory for Optoelectronic Information of China, Fuzhou 350108, China

\* Corresponding authors (emails: [zhengwei@fjirsm.ac.cn](mailto:zhengwei@fjirsm.ac.cn) (Zheng W); [xchen@fjirsm.ac.cn](mailto:xchen@fjirsm.ac.cn) (Chen X))

luminescence of  $\text{Ln}^{3+}$  from the thermally coupled CF levels [54,55].

In this work, we develop a unique strategy for the controlled synthesis of  $\text{Ln}^{3+}$ -doped SrS NCs *via* a high-temperature co-precipitation method. The optical properties, ET processes, and excited-state dynamics of  $\text{Ln}^{3+}$  in  $\text{Ce}^{3+}$  singly-doped,  $\text{Ce}^{3+}/\text{Er}^{3+}$  and  $\text{Ce}^{3+}/\text{Nd}^{3+}$  co-doped SrS NCs are systematically investigated through concentration- and temperature-dependent steady-state and transient PL spectroscopies. Through sensitization by  $\text{Ce}^{3+}$ , efficient NIR-II luminescence from  $\text{Er}^{3+}$  and  $\text{Nd}^{3+}$  is achieved for the first time in sub-10 nm SrS NCs. Furthermore, by virtue of the well-resolved CF transition lines from  $^4\text{I}_{13/2}$  of  $\text{Er}^{3+}$ , we show the potential of SrS: $\text{Ce}^{3+}/\text{Er}^{3+}$  NCs as blue-LED-excitable NIR-II luminescent nanoprobes for non-contact thermal sensing with a high sensitivity.

## EXPERIMENTAL SECTION

### Chemicals and materials

The metal acetates of  $\text{Sr}(\text{CH}_3\text{COO})_2 \cdot 0.5\text{H}_2\text{O}$  (99.9%),  $\text{Ce}(\text{CH}_3\text{COO})_3 \cdot 4\text{H}_2\text{O}$  (99.99%),  $\text{Er}(\text{CH}_3\text{COO})_3 \cdot 4\text{H}_2\text{O}$  (99.99%), and  $\text{Nd}(\text{CH}_3\text{COO})_3 \cdot 4\text{H}_2\text{O}$  (99.99%) were bought from Aladdin (China). The organic ligands of oleic acid (OA), oleylamine (OAm), 1-octadecene (ODE), and  $N,N'$ -diphenylthiourea (DPTU) were purchased from Sigma-Aldrich (China). Ethanol and cyclohexane were bought from Sinopharm (China). All chemicals were used as received without further purification.

### Synthesis of SrS: $\text{Ln}^{3+}$ NCs

Monodispersed SrS: $\text{Ln}^{3+}$  NCs were prepared *via* a co-precipitation method at an elevated temperature. For synthesizing SrS:0.1%  $\text{Ce}^{3+}$  NCs, the metal acetates including 0.999 mmol of  $\text{Sr}(\text{CH}_3\text{COO})_2 \cdot \text{H}_2\text{O}$  and 0.001 mmol of  $\text{Ce}(\text{CH}_3\text{COO})_3 \cdot 4\text{H}_2\text{O}$  (0.01 mol  $\text{L}^{-1}$  in aqueous solution, 100  $\mu\text{L}$ ) were first loaded into a 100-mL three-necked flask, followed by addition of organic ligands containing 4 mL of OA, 8 mL of OAm, and 8 mL of ODE. Then, the temperature was raised up to 120°C and the mixture was stirred at this temperature for 1 h under flowing with  $\text{N}_2$  to remove the residual water and oxygen. Thereafter, the temperature was raised up to 180°C and kept for 30 min to dissolve the metal acetates. The solution was then cooled down to RT and 3 mmol of DPTU (in 10 mL of ethanol) was added. After evaporation of ethanol at 80°C for 30 min, the solution was heated to 320°C and stirred for 1 h under  $\text{N}_2$  flow to complete the reaction. The resulting mixture was then cooled down to RT and 30 mL of ethanol was added to precipitate the products. The NCs were collected by centrifugation at 8000  $\times g$  for 6 min, and then washed with ethanol and cyclohexane (2:1 in volume) twice. The powder samples were obtained by drying the colloidal NCs at 60°C in a vacuum drying oven for 12 h.

### Characterizations

Powder X-ray diffraction (XRD) measurement was performed on the MiniFlex 600 X-ray diffractometer (Rigaku) by using Cu  $\text{K}\alpha 1$  ( $\lambda = 0.154187$  nm) as the radiation source. Transmission electron microscopy (TEM) images were acquired on a TECNAI G2 F20 TEM instrument. Inductively coupled plasma-atomic emission spectroscopy (ICP-AES, Ultima2, Jobin Yvon) and energy dispersive X-ray (EDX) spectrometer were used for the chemical composition analysis. The diffuse reflectance spectra were recorded on a UV/Vis/NIR spectrometer (Lambda 950,

Perkin-Elmer) and  $\text{BaSO}_4$  was used as the reference. The FLS980 spectrometer (Edinburgh) was employed for recording the PL excitation and emission spectra and PL decay curves of the samples. A continuous and pulsed xenon lamp (450 W) was used as the excitation source. For absolute PL quantum yield (QY) measurement, the standard barium sulfate-coated integrating sphere (150 nm in diameter, Edinburgh) was mounted on the FLS980 spectrometer and utilized as the sample chamber. The measurements were repeated for three times to produce the average value and standard deviation. For low-temperature PL measurements, a closed cycle cryostat (10–300 K, DE202, Advanced Research Systems) was used as the sample chamber, and the slits of excitation and emission monochromators were set as small as possible to maximize the instrumental resolution. All the spectral data were recorded at RT by using the powder samples unless otherwise noted and corrected for the spectral response of the instruments.

## RESULTS AND DISCUSSION

The SrS crystal has a face-centered cubic structure (space group  $Fm\bar{3}m$ ) consisting of edge-sharing  $\text{SrS}_6$  octahedra (Fig. 1a) [56].  $\text{Ln}^{3+}$  ions occupy the octahedral  $\text{Sr}^{2+}$  site, with charge compensation by  $\text{S}^{2-}$  deficiency. Monodispersed SrS: $\text{Ln}^{3+}$  NCs ( $\text{Ln} = \text{Ce}$ ,  $\text{Nd}$ , and  $\text{Er}$ ) were synthesized through a modified high-temperature co-precipitation method as we previously reported [46]. The as-synthesized NCs were hydrophobic owing to oleic ligands anchored to the surface, and thus can be readily dispersed in nonpolar organic solvents such as cyclohexane, forming a transparent colloidal solution. Upon doping with a trace amount (0.1 mol%) of  $\text{Ce}^{3+}$ , the NCs exhibited bright blue-green PL under 365-nm UV LED irradiation. XRD patterns of the NCs (Fig. 1b) display intense diffraction peaks which match well with cubic SrS (JCPDS No. 008-0489), indicating high crystallinity and phase purity of the resulting NCs. The diffraction peaks of the NCs turn broader with increasing  $\text{Ln}^{3+}$  doping concentration (Fig. S1), suggesting a size reduction of the NCs induced by  $\text{Ln}^{3+}$  doping. According to the Debye-Scherrer equation, the mean sizes of the NCs were estimated to be  $10.9 \pm 0.4$ ,  $10.4 \pm 0.7$ ,  $9.6 \pm 0.3$ , and  $9.9 \pm 0.6$  nm for SrS, SrS:0.1%  $\text{Ce}^{3+}$ , SrS:0.1%  $\text{Ce}^{3+}/0.5\%$   $\text{Er}^{3+}$ , and SrS:0.1%  $\text{Ce}^{3+}/0.2\%$   $\text{Nd}^{3+}$ , respectively. Such a size reduction induced by  $\text{Ln}^{3+}$  doping can be ascribed to the charge compensation by extra  $\text{S}^{2-}$  which introduced transient electric dipoles to the NC surface with negative poles outwards. These transient electric dipoles hindered the diffusion of  $\text{S}^{2-}$  ions from the solution to the grain surface, thus retarding the growth of SrS NCs [57]. TEM images show that the NCs are monodispersed and roughly spherical with mean sizes of  $10.4 \pm 1.1$ ,  $10.4 \pm 0.9$ ,  $9.5 \pm 0.9$ , and  $9.7 \pm 0.9$  nm for SrS, SrS:0.1%  $\text{Ce}^{3+}$ , SrS:0.1%  $\text{Ce}^{3+}/0.5\%$   $\text{Er}^{3+}$ , and SrS:0.1%  $\text{Ce}^{3+}/0.2\%$   $\text{Nd}^{3+}$  NCs, respectively (Fig. 1c–f and Fig. S2), in good agreement with those determined by XRD measurements. The representative high-resolution TEM (HRTEM) image of the NCs (inset of Fig. 1c) exhibits clear lattice fringes with an observed  $d$  spacing of 0.21 nm, corresponding to the (220) plane of cubic SrS. The selected-area electron diffraction (SAED) pattern of the NCs shows intense diffraction rings that can be well indexed into cubic SrS (inset of Fig. 1f). Composition analyses through EDX spectrum and ICP-AES identify the elements of Sr and S and 0.13 mol% of  $\text{Ce}^{3+}$  dopants in SrS:0.1%  $\text{Ce}^{3+}$  NCs (Fig. S3). All these results reveal high quality of the as-synthesized  $\text{Ln}^{3+}$ -doped SrS NCs.

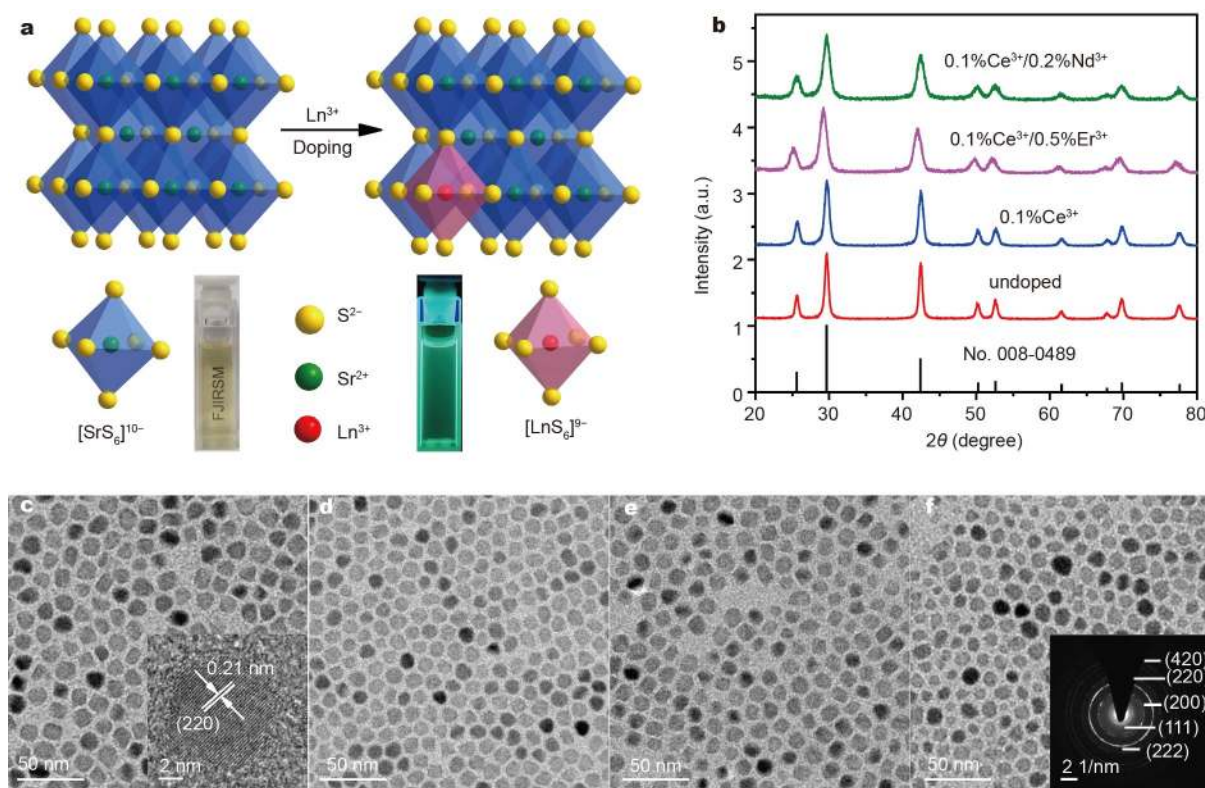


**Figure 1** (a) Arrangement of strontium and sulphur atoms in the SrS structure and the crystallographic site for Ln<sup>3+</sup> dopants. The photographs for the cyclohexane solution (1 mg mL<sup>-1</sup>) of SrS:0.1% Ce<sup>3+</sup> NCs under (left) ambient light and (right) 365-nm UV light are presented, showing transparency of the colloidal solution and its bright blue-green PL under UV light. (b) Powder XRD patterns of SrS, SrS:0.1% Ce<sup>3+</sup>, SrS:0.1% Ce<sup>3+</sup>/0.5% Er<sup>3+</sup>, and SrS:0.1% Ce<sup>3+</sup>/0.2% Nd<sup>3+</sup> NCs. The vertical lines in the bottom represent the standard pattern of cubic SrS (JCPDS No. 008-0489). TEM images of (c) SrS, (d) SrS:0.1% Ce<sup>3+</sup>, (e) SrS:0.1% Ce<sup>3+</sup>/0.5% Er<sup>3+</sup>, and (f) SrS:0.1% Ce<sup>3+</sup>/0.2% Nd<sup>3+</sup> NCs. The insets show the corresponding HRTEM image and SAED pattern of the NCs.

Optical absorption spectra show that the NCs have large absorbance in the UV region with a maximum at around 252 nm and a long absorption tail extending to 600 nm (Fig. S4). From the Tauc plot of the absorption spectra, the bandgap of the undoped SrS NCs was estimated to be 4.2 eV, which is generally consistent with that (4.3 eV) of bulk SrS [58]. Upon 0.1 mol% of Ce<sup>3+</sup> doping, an additional absorption band at around 430 nm was explicitly observed, which can be assigned to the 4f→5d transition of octahedral Ce<sup>3+</sup> in SrS NCs [59]. Under excitation at 410 nm, Ce<sup>3+</sup> singly-doped NCs exhibited bright blue-green PL with two broad emission bands at 478 and 530 nm (Fig. 2a), corresponding to the electronic transitions of Ce<sup>3+</sup> from the lowest <sup>2</sup>T<sub>2g</sub> level of the 5d state to the <sup>2</sup>F<sub>5/2</sub> and <sup>2</sup>F<sub>7/2</sub> levels of the 4f ground state, respectively [59]. By monitoring the Ce<sup>3+</sup> emission at 530 nm, two intense excitation bands at 263 and 430 nm were observed, ascribing to the host absorption of SrS and the 4f→5d transition of Ce<sup>3+</sup>, respectively [53]. Furthermore, it was observed that the PL intensity of the NCs increased gradually with increasing Ce<sup>3+</sup> concentration from 0.01 to 0.1 mol% and then decreased at higher Ce<sup>3+</sup> concentrations, indicative of an extremely low quenching concentration (0.1 mol%) of Ce<sup>3+</sup> in SrS NCs. When the Ce<sup>3+</sup> concentration exceeded 0.5 mol%, the emission bands of Ce<sup>3+</sup> were red-shifted and broadened significantly, due to ET from Ce<sup>3+</sup> ions emitting at higher energy to slightly perturbed Ce<sup>3+</sup> ions emitting at lower energies [60], as also evidenced by the decreased PL lifetime of Ce<sup>3+</sup> from 4.5 ns (0.1 mol%) to 3.9 ns (1 mol%) with increasing Ce<sup>3+</sup> concentration (Fig. 2b and Table S1). The absolute PLQY

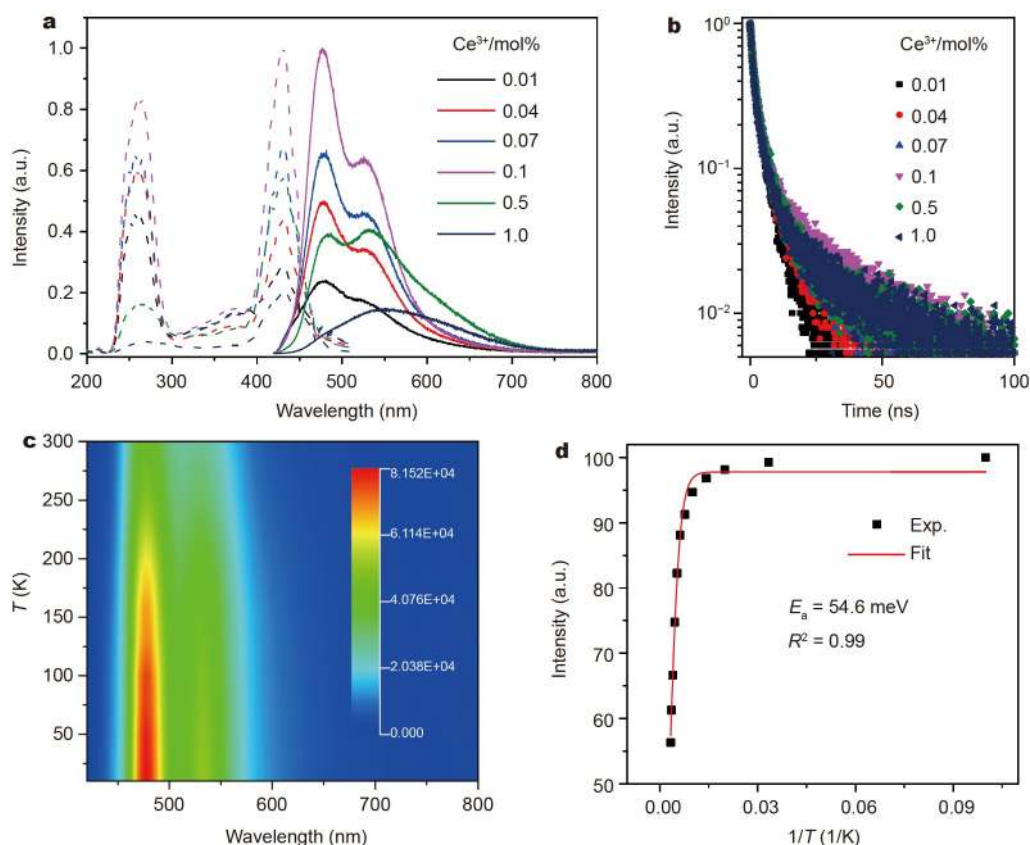
was determined to be 6.1% ± 0.1% for SrS:0.1% Ce<sup>3+</sup> NCs, which is higher than that (~2.9%) of 10.2-nm CaS:Ce<sup>3+</sup> NCs we previously reported [46]. In comparison with CaS, the SrS host exerts weaker covalency and CF strength on Ce<sup>3+</sup> ions due to the higher metallicity of Sr<sup>2+</sup> than Ca<sup>2+</sup>. Therefore, the 5d state of Ce<sup>3+</sup> locates at higher energies in SrS than in CaS, which results in a blueshift in the emission bands of Ce<sup>3+</sup> (478 and 530 nm) in SrS relative to that (505 and 565 nm) in CaS (Fig. S5). As such, Ce<sup>3+</sup> ions are less affected by the surface quenching effect and have a higher PLQY in SrS NCs than in CaS NCs with a similar size.

Fig. 2c and Fig. S6 show the temperature-dependent PL emission spectra (10–300 K) of SrS:0.1% Ce<sup>3+</sup> NCs under excitation at 410 nm. The PL intensity of the NCs decreased gradually with the temperature rises due to the accelerated nonradiative relaxation and enhanced electron-phonon coupling of Ce<sup>3+</sup> at higher temperatures [61], as further verified by the decreased PL lifetime of Ce<sup>3+</sup> from 9.1 to 5.0 ns with elevating the temperature from 10 to 300 K (Fig. S7 and Table S2). Based on the Arrhenius plot of the integrated PL intensity of Ce<sup>3+</sup> versus the inverse temperature (Fig. 2d) [62]:

$$I(T) = \frac{I_0}{1 + A \exp(-E_a/k_B T)}, \quad (1)$$

where  $I(T)$  and  $I_0$  are the integrated PL intensities at  $T$  and 0 K, respectively,  $E_a$  is the activation energy, and  $k_B$  is the Boltzmann constant. The activation energy was determined to be 54.6 meV. The relatively small activation energy of Ce<sup>3+</sup> in SrS NCs, along





**Figure 2** (a) PL excitation spectra (dash line,  $\lambda_{\text{em}} = 530$  nm), PL emission spectra (solid line,  $\lambda_{\text{ex}} = 410$  nm), and (b) PL decay curves ( $\lambda_{\text{em}} = 530$  nm) of SrS: $x\%$  Ce<sup>3+</sup> NCs with different Ce<sup>3+</sup> concentrations. (c) Wavelength-temperature contour plot of the temperature-dependent PL emission spectra of SrS:0.1% Ce<sup>3+</sup> NCs under excitation at 410 nm. (d) Integrated PL intensity for the Ce<sup>3+</sup> emission as a function of temperature, whereby the activation energy ( $E_a$ ) for the Ce<sup>3+</sup> emission in SrS:0.1% Ce<sup>3+</sup> NCs was derived.

with the high covalency and volatility of S<sup>2-</sup> which result in abundant S<sup>2-</sup> deficiency in the NCs [63], may account for the low quenching concentration (0.1 mol%) of Ce<sup>3+</sup> in SrS NCs.

In addition to that of Ce<sup>3+</sup> singly-doped SrS NCs, we also investigated the optical properties of Ce<sup>3+</sup>/Nd<sup>3+</sup> and Ce<sup>3+</sup>/Er<sup>3+</sup> co-doped SrS NCs. As shown in Fig. 3a, upon excitation to the Ce<sup>3+</sup> 5d state at 430 nm, characteristic and sharp emission peaks from the <sup>4</sup>F<sub>3/2</sub>→<sup>4</sup>I<sub>J</sub> transitions of Nd<sup>3+</sup> in NIR-I (700–950 nm) at 890 nm (<sup>4</sup>I<sub>9/2</sub>) and NIR-II at 1081 nm (<sup>4</sup>I<sub>11/2</sub>) and 1354 nm (<sup>4</sup>I<sub>13/2</sub>) were detected in Ce<sup>3+</sup>/Nd<sup>3+</sup> co-doped SrS NCs, along with the blue-green emission of Ce<sup>3+</sup> at 478 and 530 nm. The PL intensity of Nd<sup>3+</sup> increased gradually with increasing Nd<sup>3+</sup> concentrations from 0 to 0.2 mol% and then decreased at higher Nd<sup>3+</sup> concentrations owing to the concentration quenching effect [64], with the effective PL lifetime of Nd<sup>3+</sup> decreasing from 3.6 ms (0.01 mol%) to 0.2 ms (2 mol%) (Fig. 3b and Table S3). Meanwhile, the PL intensity of Ce<sup>3+</sup> decreased significantly with increasing Nd<sup>3+</sup> concentration, indicating an efficient ET from Ce<sup>3+</sup> to Nd<sup>3+</sup> in the NCs. Such Ce<sup>3+</sup>-to-Nd<sup>3+</sup> ET was further confirmed by the nearly identical excitation bands for the Ce<sup>3+</sup> and Nd<sup>3+</sup> emissions and the decreased PL lifetime of Ce<sup>3+</sup> from 4.5 to 3.1 ns when the Nd<sup>3+</sup> concentration increased from 0 to 2 mol% (Fig. 3c, d). From the PL lifetime of Ce<sup>3+</sup>, the efficiency of ET from Ce<sup>3+</sup> to Nd<sup>3+</sup> was calculated, with the highest value of 31.1% in SrS:0.1% Ce<sup>3+</sup>/2% Nd<sup>3+</sup> NCs (Table S3). Fig. 3e depicts the ET processes from Ce<sup>3+</sup> to Nd<sup>3+</sup> in SrS NCs. Upon excitation

at 430 nm, the Ce<sup>3+</sup> ion is excited to the 5d state, and then ET occurs from the lowest <sup>2</sup>T<sub>2g</sub> level of the Ce<sup>3+</sup> 5d state to the <sup>4</sup>G<sub>5/2</sub>/<sup>4</sup>G<sub>7/2</sub> levels of Nd<sup>3+</sup>, followed by nonradiative relaxation to <sup>4</sup>F<sub>3/2</sub> of Nd<sup>3+</sup> which results in intense NIR emission of Nd<sup>3+</sup> through <sup>4</sup>F<sub>3/2</sub>→<sup>4</sup>I<sub>J</sub> ( $J = 9/2, 11/2$ , and  $13/2$ ) transitions.

Similarly, upon excitation at 430 nm, both the Ce<sup>3+</sup> emission at 478 and 530 nm and the typical NIR-II emission from the <sup>4</sup>I<sub>13/2</sub>→<sup>4</sup>I<sub>15/2</sub> transition of Er<sup>3+</sup> at 1539 nm were observed in Ce<sup>3+</sup>/Er<sup>3+</sup> co-doped SrS NCs (Fig. 4a). The PL intensity of Er<sup>3+</sup> underwent a gradual increase with increasing Er<sup>3+</sup> concentration from 0.01 to 0.5 mol% and then decreased at higher Er<sup>3+</sup> concentrations at the expense of Ce<sup>3+</sup> emission, as a result of efficient ET from Ce<sup>3+</sup> to Er<sup>3+</sup>. Accordingly, the effective PL lifetimes of Er<sup>3+</sup> and Ce<sup>3+</sup> decreased from 13.0 ms (0.01 mol%) and 4.5 ns to 0.3 ms and 2.3 ns, respectively, as the Er<sup>3+</sup> concentration increased from 0 to 5 mol% (Fig. 4b, c), due to the concentration quenching effect of Er<sup>3+</sup> and Ce<sup>3+</sup>-to-Er<sup>3+</sup> ET. PL excitation spectra of the NCs by monitoring the Er<sup>3+</sup> emission at 1539 nm and the Ce<sup>3+</sup> emission at 530 nm exhibited nearly identical excitation bands from the host absorption of SrS and the 4f→5d transition of Ce<sup>3+</sup> (Fig. 4d), confirming the efficient Ce<sup>3+</sup>-to-Er<sup>3+</sup> ET. From the PL lifetime of Ce<sup>3+</sup>, the efficiency of ET from Ce<sup>3+</sup> to Er<sup>3+</sup> was calculated, with the highest value of 48.9% in SrS:0.1% Ce<sup>3+</sup>/5% Er<sup>3+</sup> NCs (Table S4). By contrast, negligibly weak PL was detected in Er<sup>3+</sup> (or Nd<sup>3+</sup>) singly-doped SrS NCs. These results demonstrate unambiguously that it is the allowed 4f→5d tran-

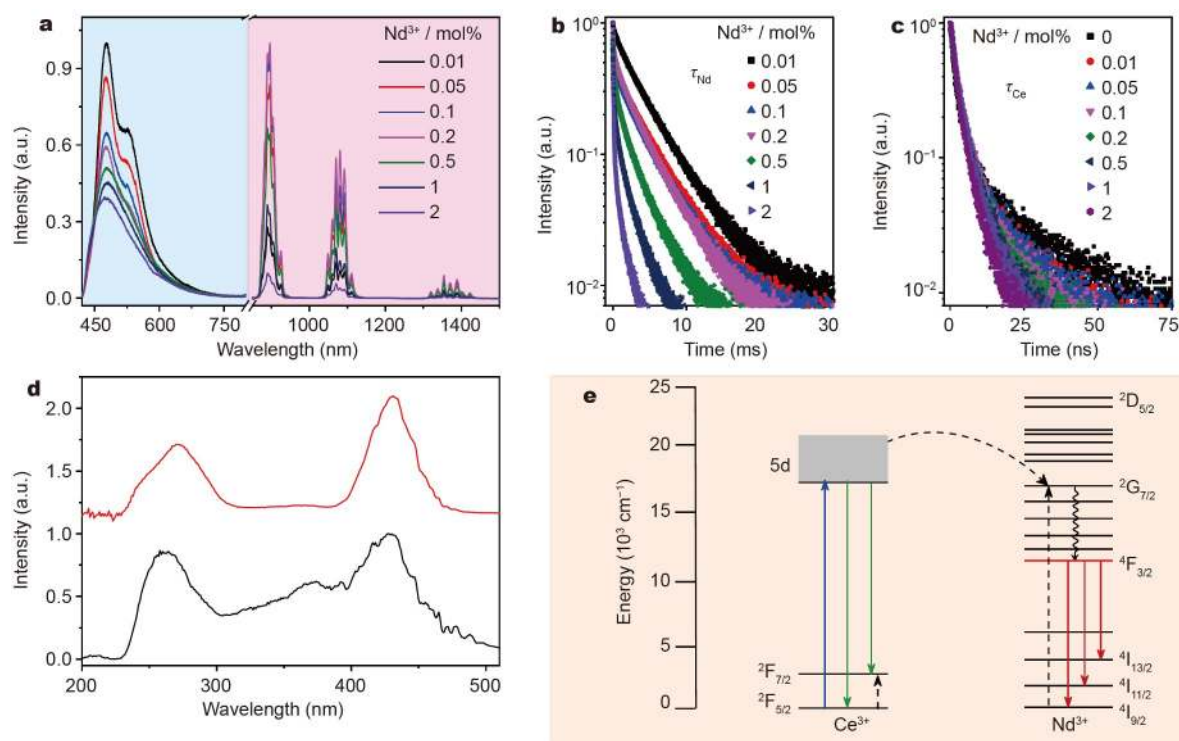


**Figure 3** (a) Nd<sup>3+</sup> concentration-dependent PL emission spectra ( $\lambda_{\text{ex}} = 430$  nm), and PL decay curves from (b)  $^4\text{F}_{3/2}$  level of Nd<sup>3+</sup> ( $\lambda_{\text{em}} = 1081$  nm) and (c) 5d state of Ce<sup>3+</sup> ( $\lambda_{\text{em}} = 530$  nm) in SrS:0.1% Ce<sup>3+</sup>/x% Nd<sup>3+</sup> NCs. (d) PL excitation spectra of SrS:0.1% Ce<sup>3+</sup>/0.2% Nd<sup>3+</sup> NCs by monitoring the Ce<sup>3+</sup> (black) and Nd<sup>3+</sup> (red) emissions at 530 and 1081 nm, respectively, showing the typical excitation bands from the host absorption of SrS and the 4f→5d transition of Ce<sup>3+</sup> for both Ce<sup>3+</sup> and Nd<sup>3+</sup> emissions. (e) Simplified energy level schemes for Ce<sup>3+</sup> and Nd<sup>3+</sup> in SrS NCs, showing the proposed ET processes from Ce<sup>3+</sup> to Nd<sup>3+</sup>. The dashed, curve, and full arrows represent the ET, nonradiative relaxation and radiative transition processes, respectively.

sition of Ce<sup>3+</sup> which harvests the excitation light and then sensitizes the NIR-II luminescence of Er<sup>3+</sup> and Nd<sup>3+</sup> in Ce<sup>3+</sup>/Er<sup>3+</sup> and Ce<sup>3+</sup>/Nd<sup>3+</sup> co-doped SrS NCs. As illustrated in Fig. 4e, upon excitation to the 5d state of Ce<sup>3+</sup>, the excitation energy is transferred from the lowest  $^2\text{T}_{2g}$  level of Ce<sup>3+</sup> to the  $^2\text{H}_{11/2}/^4\text{S}_{3/2}$  levels of Er<sup>3+</sup>, followed by nonradiative (or radiative) relaxation to  $^4\text{I}_{13/2}$  of Er<sup>3+</sup> which leads to intense NIR-II emission of Er<sup>3+</sup> through  $^4\text{I}_{13/2} \rightarrow ^4\text{I}_{15/2}$  transition. The PLQYs for the NIR-II emissions of Er<sup>3+</sup> and Nd<sup>3+</sup> sensitized by Ce<sup>3+</sup> were estimated to be  $2.9\% \pm 0.1\%$  in SrS:0.1% Ce<sup>3+</sup>/0.5% Er<sup>3+</sup> and  $2.3\% \pm 0.1\%$  in SrS:0.1% Ce<sup>3+</sup>/0.2% Nd<sup>3+</sup> NCs. It is worth mentioning that, despite its currently low internal PLQYs, the NIR-II PL of Er<sup>3+</sup> and Nd<sup>3+</sup> sensitized by the allowed 4f→5d transition of Ce<sup>3+</sup> in SrS NCs is much stronger than that in fluorides such as NaYF<sub>4</sub>:Yb<sup>3+</sup>/Er<sup>3+</sup> NCs via excitation based on the forbidden 4f→4f transitions.

To gain deep insights into the ET processes from Ce<sup>3+</sup> to Er<sup>3+</sup> and Nd<sup>3+</sup> in Ce<sup>3+</sup>/Er<sup>3+</sup> and Ce<sup>3+</sup>/Nd<sup>3+</sup> co-doped SrS NCs, we carried out temperature-dependent steady-state and transient PL spectroscopic measurements. Fig. 5a shows the temperature-dependent PL emission spectra (10–300 K) of SrS:0.1% Ce<sup>3+</sup>/0.5% Er<sup>3+</sup> NCs under excitation at 430 nm. It was observed that the integrated PL intensity and PL lifetime for the blue-green emission of Ce<sup>3+</sup> decreased gradually with increasing the temperature from 10 to 300 K (Fig. S8 and Table S5), due mainly to larger nonradiative transition probability of Ce<sup>3+</sup> at higher temperatures, as also observed in Ce<sup>3+</sup> singly-doped SrS NCs. For comparison, the integrated PL intensity for the NIR-II emission of Er<sup>3+</sup> exhibited a slight decrease with increasing

temperature from 10 to 100 K and then increased steadily with the temperature rise (Fig. 5b), in parallel with the essentially unchanged PL lifetime of 6.5 ms (Fig. S9). Such a temperature evolution in PL intensity and PL lifetime of Er<sup>3+</sup> in SrS:Ce<sup>3+</sup>/Er<sup>3+</sup> NCs was different from those of Nd<sup>3+</sup> in SrS:Ce<sup>3+</sup>/Nd<sup>3+</sup> NCs, wherein both the PL intensities and PL lifetimes of Ce<sup>3+</sup> and Nd<sup>3+</sup> decreased significantly with the temperature rise (Fig. S10 and Table S6). This implies a phonon-assisted ET process from Ce<sup>3+</sup> to Er<sup>3+</sup> in SrS:Ce<sup>3+</sup>/Er<sup>3+</sup> NCs, in view of the increased occupation number of the phonon state at higher temperatures [65].

Coincidentally, we found that the intensities for the  $^4\text{I}_{13/2} \rightarrow ^4\text{I}_{15/2}$  CF transition lines of Er<sup>3+</sup> experienced drastically distinct temperature dependence. Because of the increased occupation number of the phonon state at higher temperatures, the high-lying CF sublevel ( $R_2$ ) of  $^4\text{I}_{13/2}$  of Er<sup>3+</sup> will be thermally populated from the low-lying one ( $R_1$ ) with increasing temperature [54]. As a result, the intensities for the CF transitions of Er<sup>3+</sup> from  $R_2$  of  $^4\text{I}_{13/2}$  to the higher-lying CF sublevels of  $^4\text{I}_{15/2}$  at 1551 and 1554 nm showed an increase with the temperature rise, whereas those from  $R_1$  of  $^4\text{I}_{13/2}$  to the lower-lying CF sublevels of  $^4\text{I}_{15/2}$  at 1534, 1539, 1541, and 1544 nm decreased (inset of Fig. 5a). It is difficult to accurately identify all the  $^4\text{I}_{13/2} \rightarrow ^4\text{I}_{15/2}$  CF transition lines of Er<sup>3+</sup> in SrS NCs, because of the negligibly weak PL upon direct excitation to Er<sup>3+</sup> based on the forbidden 4f→4f transitions. Nonetheless, the CF emission peaks of Er<sup>3+</sup> at 1539 and 1554 nm, which exhibit opposite temperature dependence in intensity (Fig. 5c), are sharp and well-resolved with little interference from other Stark components at temperatures below

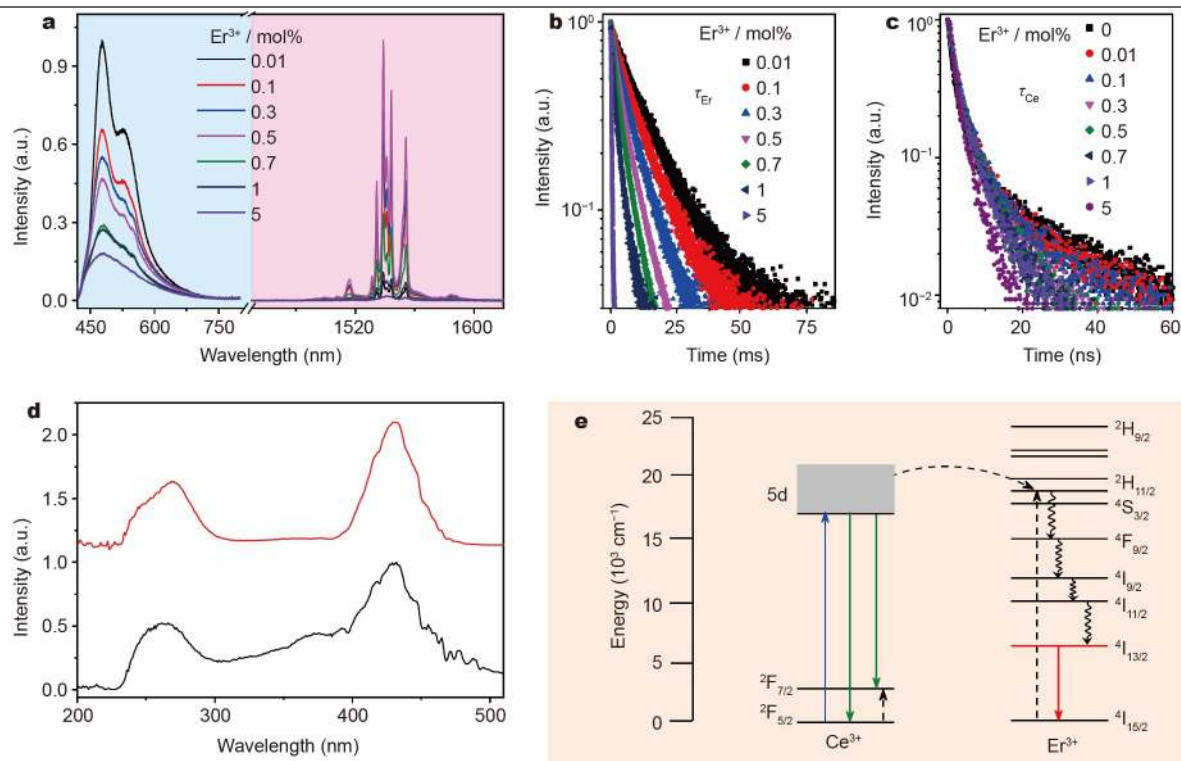


**Figure 4** (a)  $\text{Er}^{3+}$  concentration-dependent PL emission spectra ( $\lambda_{\text{ex}} = 430 \text{ nm}$ ), and PL decay curves from (b)  $^4\text{I}_{13/2}$  level of  $\text{Er}^{3+}$  ( $\lambda_{\text{em}} = 1539 \text{ nm}$ ) and (c)  $5\text{d}$  state of  $\text{Ce}^{3+}$  ( $\lambda_{\text{em}} = 530 \text{ nm}$ ) in  $\text{SrS}:0.1\% \text{Ce}^{3+}/x\% \text{Er}^{3+}$  NCs. (d) PL excitation spectra of  $\text{SrS}:0.1\% \text{Ce}^{3+}/0.5\% \text{Er}^{3+}$  NCs by monitoring the  $\text{Ce}^{3+}$  (black) and  $\text{Er}^{3+}$  (red) emissions at 530 and 1539 nm, respectively, showing the typical excitation bands from the host absorption of SrS and the  $4\text{f} \rightarrow 5\text{d}$  transition of  $\text{Ce}^{3+}$  for both  $\text{Ce}^{3+}$  and  $\text{Er}^{3+}$  emissions. (e) Simplified energy level schemes for  $\text{Ce}^{3+}$  and  $\text{Er}^{3+}$  in SrS NCs, showing the proposed ET processes from  $\text{Ce}^{3+}$  to  $\text{Er}^{3+}$ . The dashed, curve, and full arrows represent the ET, nonradiative relaxation and radiative transition processes, respectively.

300 K. This feature makes  $\text{SrS}:\text{Ce}^{3+}/\text{Er}^{3+}$  NCs an ideal nanoprobe candidate for ratiometric temperature sensing based on the temperature-dependent fluorescent intensity ratio (FIR) of  $\text{Er}^{3+}$  at 1554 and 1539 nm ( $I_{1554}/I_{1539}$ ).

As shown in Fig. 5d, the FIR of  $I_{1554}/I_{1539}$  increased remarkably from 0.17 to 0.60 with increasing the temperature from 10 to 300 K, as a result of enhanced thermal population of the  $R_2$  sublevel from  $R_1$  of  $^4\text{I}_{13/2}$  of  $\text{Er}^{3+}$  at higher temperatures. According to the theory of Boltzmann distribution, the FIR of the thermally coupled Stark sublevels ( $R_1$  and  $R_2$ ) of  $^4\text{I}_{13/2}$  can be expressed as [66]

$$\text{FIR} = \frac{I_{1554}}{I_{1539}} = C \exp\left(-\frac{\Delta E}{k_B T}\right), \quad (2)$$

where  $C$  is a constant dictated by the radiative transition rates, degeneracies and the emission cross-sections of  $R_1$  and  $R_2$  sublevels, and  $\Delta E$  represents the energy gap between  $R_1$  and  $R_2$ . As a consequence, the natural logarithm of the FIR displayed a linear relationship with the inverse temperature (Fig. 5e). By linear fitting to the plot, the energy gap  $\Delta E$  and the constant  $C$  were calculated to be  $87.7 \text{ cm}^{-1}$  and 0.90, respectively. The temperature sensitivity ( $S$ ) of the nanoprobe, defined as the rate of FIR change versus temperature change, is expressed as [67]

$$S(T) = \frac{d(\text{FIR})}{dT} = C \left( \frac{\Delta E}{k_B T^2} \right) \exp\left(-\frac{\Delta E}{k_B T}\right). \quad (3)$$

By taking the values of  $C$  and  $\Delta E$  into Equation (3), the sensitivity function  $S(T)$  versus  $T$  was derived and plotted in Fig. 5f. Typically, the maximum  $S$  value of  $0.33\% \text{ K}^{-1}$  was achieved at

100 K, which is comparable to that of thermal sensing based on  $\text{Er}^{3+}$ -activated upconversion nanoprobe [68–70]. The high temperature sensitivity, along with the large absorbance of  $\text{Ce}^{3+}$  at 430 nm and the NIR-II emission of  $\text{Er}^{3+}$  in the optical communication window, enables  $\text{SrS}:\text{Ce}^{3+}/\text{Er}^{3+}$  NCs as blue-LED-excitable NIR-II luminescent nanoprobe for cryogenic temperature sensing in space and energy exploration [71–73].

## CONCLUSIONS

In summary, we have systematically investigated  $\text{Ln}^{3+}$ -doped SrS NCs from the controlled synthesis and optical properties to their potential application as a ratiometric temperature sensor. Upon doping with a trace amount (0.1 mol%) of  $\text{Ce}^{3+}$ , the NCs exhibited bright blue-green PL at 478 and 530 nm with a PLQY of 6.1%. Through sensitization by the allowed  $4\text{f} \rightarrow 5\text{d}$  transition of  $\text{Ce}^{3+}$  in the blue region, intense NIR-II luminescence from  $\text{Er}^{3+}$  at 1539 nm and  $\text{Nd}^{3+}$  at 1081 nm with PLQYs of 2.9% and 2.3%, respectively, was achieved in  $\text{Ce}^{3+}/\text{Er}^{3+}$  and  $\text{Ce}^{3+}/\text{Nd}^{3+}$  co-doped SrS NCs. By means of temperature-dependent steady-state and transient PL spectroscopies, a phonon-assisted ET from  $\text{Ce}^{3+}$  to  $\text{Er}^{3+}$  was unveiled. Furthermore, owing to the strong CF level splitting exerted by SrS, the  $\text{Er}^{3+}$  luminescence was characterized by sharp and well-resolved CF emission peaks, which enables  $\text{SrS}:\text{Ce}^{3+}/\text{Er}^{3+}$  NCs as blue-LED-excitable NIR-II luminescent nanoprobe for non-contact temperature detection based on the thermally coupled Stark sublevels of  $^4\text{I}_{13/2}$  of  $\text{Er}^{3+}$ . These findings provide fundamental insights into the optical properties and excited-state dynamics of  $\text{Ln}^{3+}$  in SrS NCs, thus



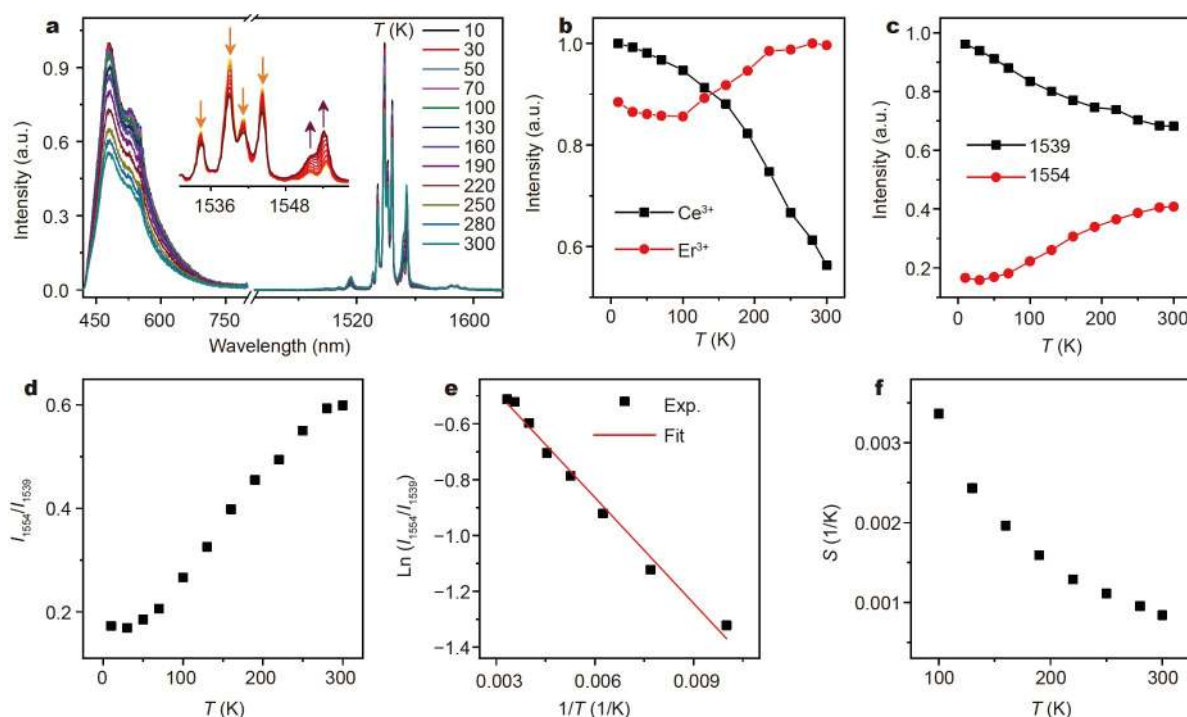


**Figure 5** (a) Temperature-dependent PL emission spectra ( $\lambda_{\text{ex}} = 430$  nm) of SrS:0.1%  $\text{Ce}^{3+}$ /0.5%  $\text{Er}^{3+}$  NCs. The inset enlarges the  $^4\text{I}_{13/2} \rightarrow ^4\text{I}_{15/2}$  CF transitions of  $\text{Er}^{3+}$ , showing drastically different temperature dependence for the CF transition lines of  $\text{Er}^{3+}$ . Integrated PL intensities for (b) the green emission of  $\text{Ce}^{3+}$ , the NIR-II emission of  $\text{Er}^{3+}$ , and (c) the  $^4\text{I}_{13/2} \rightarrow ^4\text{I}_{15/2}$  CF transitions of  $\text{Er}^{3+}$  at 1539 and 1554 nm as a function of temperature. (d) PL intensity ratio between the CF emission peaks of  $\text{Er}^{3+}$  at 1554 and 1539 nm ( $I_{1554}/I_{1539}$ ) as a function of temperature. (e) Plot of the FIR of  $I_{1554}/I_{1539}$  versus the inverse temperature. (f) The temperature sensitivity ( $S$ ) of SrS: $\text{Ce}^{3+}/\text{Er}^{3+}$  nanoprobe as a function of temperature.

laying a foundation for future design of novel NIR-II luminescent nanoprobe based on  $\text{Ln}^{3+}$ -doped sulphides for applications such as deep-tissue temperature detection.

Received 13 August 2021; accepted 16 September 2021;  
published online 2 November 2021

- Sun Z, Huang H, Zhang R, *et al.* Activatable rare earth near-infrared-II fluorescence ratiometric nanoprobe. *Nano Lett*, 2021, 21: 6576–6583
- Li H, Wang X, Ohulchanskyy TY, *et al.* Lanthanide-doped near-infrared nanoparticles for biophotonics. *Adv Mater*, 2021, 33: 2000678
- Zhong Y, Dai H. A mini-review on rare-earth down-conversion nanoparticles for NIR-II imaging of biological systems. *Nano Res*, 2020, 13: 1281–1294
- Lei P, Feng J, Zhang H. Emerging biomaterials: Taking full advantage of the intrinsic properties of rare earth elements. *Nano Today*, 2020, 35: 100952
- Li Z, Ding X, Cong H, *et al.* Recent advances on inorganic lanthanide-doped NIR-II fluorescence nanoprobe for bioapplication. *J Lumin*, 2020, 228: 117627
- Fan Y, Zhang F. A new generation of NIR-II probes: Lanthanide-based nanocrystals for bioimaging and biosensing. *Adv Opt Mater*, 2019, 7: 1801417
- Gu Y, Guo Z, Yuan W, *et al.* High-sensitivity imaging of time-domain near-infrared light transducer. *Nat Photonics*, 2019, 13: 525–531
- Xu J, Gulzar A, Yang P, *et al.* Recent advances in near-infrared emitting lanthanide-doped nanoconstructs: Mechanism, design and application for bioimaging. *Coord Chem Rev*, 2019, 381: 104–134
- Cai Y, Wei Z, Song C, *et al.* Optical nano-agents in the second near-infrared window for biomedical applications. *Chem Soc Rev*, 2019, 48: 22–37
- Li D, He S, Wu Y, *et al.* Excretable lanthanide nanoparticle for biomedical imaging and surgical navigation in the second near-infrared window. *Adv Sci*, 2019, 6: 1902042
- Skripka A, Morinvil A, Matulionyte M, *et al.* Advancing neodymium single-band nanothermometry. *Nanoscale*, 2019, 11: 11322–11330
- Yu S, Tu D, Lian W, *et al.* Lanthanide-doped near-infrared II luminescent nanoprobe for bioapplications. *Sci China Mater*, 2019, 62: 1071–1086
- Ren F, Liu H, Zhang H, *et al.* Engineering NIR-IIb fluorescence of Er-based lanthanide nanoparticles for through-skull targeted imaging and imaging-guided surgery of orthotopic glioma. *Nano Today*, 2020, 34: 100905
- Bai G, Lyu Y, Wu Z, *et al.* Lanthanide near-infrared emission and energy transfer in layered  $\text{WS}_2/\text{MoS}_2$  heterostructure. *Sci China Mater*, 2020, 63: 575–581
- Gao C, Han Y, Zhang K, *et al.* Templated-construction of hollow  $\text{MoS}_2$  architectures with improved photoresponses. *Adv Sci*, 2020, 7: 2002444
- Jia M, Fu Z, Liu G, *et al.* NIR-II/III luminescence ratiometric nanothermometry with phonon-tuned sensitivity. *Adv Opt Mater*, 2020, 8: 1901173
- Xu J, Shi R, Chen G, *et al.* All-in-one theranostic nanomedicine with ultrabright second near-infrared emission for tumor-modulated bioimaging and chemodynamic/photodynamic therapy. *ACS Nano*, 2020, 14: 9613–9625
- Yang J, He S, Hu Z, *et al.* In vivo multifunctional fluorescence imaging using liposome-coated lanthanide nanoparticles in near-infrared-II/III windows. *Nano Today*, 2021, 38: 101120
- Nexha A, Carvajal JJ, Pujol MC, *et al.* Lanthanide doped luminescence nanothermometers in the biological windows: Strategies and applications. *Nanoscale*, 2021, 13: 7913–7987
- Chen R, Zhou X, Wu Y, *et al.* NIR-II emissive lateral flow immunoassay for accurate determination of tumor marker in hemolysis. *Sens Actuat B-Chem*, 2021, 328: 129050
- Wang T, Wang S, Liu Z, *et al.* A hybrid erbium(III)-bacteriochlorin near-infrared probe for multiplexed biomedical imaging. *Nat Mater*, 2021, doi: 10.1038/s41563-021-01063-7

- 22 Xu M, Zou X, Su Q, *et al.* Ratiometric nanothermometer *in vivo* based on triplet sensitized upconversion. *Nat Commun*, 2018, 9: 2698
- 23 Han S, Deng R, Gu Q, *et al.* Lanthanide-doped inorganic nanoparticles turn molecular triplet excitons bright. *Nature*, 2020, 587: 594–599
- 24 Ding S, Lu L, Fan Y, *et al.* Recent progress in NIR-II emitting lanthanide-based nanoparticles and their biological applications. *J Rare Earths*, 2020, 38: 451–463
- 25 Ji Y, Xu W, Ding N, *et al.* Huge upconversion luminescence enhancement by a cascade optical field modulation strategy facilitating selective multispectral narrow-band near-infrared photodetection. *Light Sci Appl*, 2020, 9: 184
- 26 Lei Z, Zhang F. Molecular engineering of NIR-II fluorophores for improved biomedical detection. *Angew Chem Int Ed*, 2021, 60: 16294–16308
- 27 Wang C, Lin H, Ge X, *et al.* Dye-sensitized downconversion nanoparticles with emission beyond 1500 nm for ratiometric visualization of cancer redox state. *Adv Funct Mater*, 2021, 31: 2009942
- 28 Yang Y, Tu D, Zhang Y, *et al.* Recent advances in design of lanthanide-containing NIR-II luminescent nanoprobe. *iScience*, 2021, 24: 102062
- 29 Huang J, Pu K. Activatable molecular probes for second near-infrared fluorescence, chemiluminescence, and photoacoustic imaging. *Angew Chem Int Ed*, 2020, 59: 11717–11731
- 30 Zhang H, Chen ZH, Liu X, *et al.* A mini-review on recent progress of new sensitizers for luminescence of lanthanide doped nanomaterials. *Nano Res*, 2020, 13: 1795–1809
- 31 Bao G, Wen S, Lin G, *et al.* Learning from lanthanide complexes: The development of dye-lanthanide nanoparticles and their biomedical applications. *Coord Chem Rev*, 2021, 429: 213642
- 32 George MR, Critchley PE, Whitehead GFS, *et al.* Modified pyridine-2,6-dicarboxylate acid ligands for sensitization of near-infrared luminescence from lanthanide ions ( $\text{Ln}^{3+} = \text{Pr}^{3+}, \text{Nd}^{3+}, \text{Gd}^{3+}, \text{Dy}^{3+}, \text{Er}^{3+}$ ). *J Lumin*, 2021, 230: 117715
- 33 Wang Q, Liang T, Wu J, *et al.* Dye-sensitized rare earth-doped nanoparticles with boosted NIR-IIb emission for dynamic imaging of vascular network-related disorders. *ACS Appl Mater Interfaces*, 2021, 13: 29303–29312
- 34 Zheng W, Tu D, Huang P, *et al.* Time-resolved luminescent biosensing based on inorganic lanthanide-doped nanoprobe. *Chem Commun*, 2015, 51: 4129–4143
- 35 Huang P, Zheng W, Gong Z, *et al.* Rare earth ion- and transition metal ion-doped inorganic luminescent nanocrystals: From fundamentals to biotransformation. *Mater Today Nano*, 2019, 5: 100031
- 36 Li Y, Zhang P, Ning H, *et al.* Emitting/sensitizing ions spatially separated lanthanide nanocrystals for visualizing tumors simultaneously through up- and down-conversion near-infrared II luminescence *in vivo*. *Small*, 2019, 15: 1905344
- 37 Li Z, Wu J, Wang Q, *et al.* A universal strategy to construct lanthanide-doped nanoparticles-based activable NIR-II luminescence probe for bioimaging. *iScience*, 2020, 23: 100962
- 38 Gao Y, Li R, Zheng W, *et al.* Broadband NIR photostimulated luminescence nanoprobe based on  $\text{CaS}:\text{Eu}^{2+}, \text{Sm}^{3+}$  nanocrystals. *Chem Sci*, 2019, 10: 5452–5460
- 39 Wu Y, Fang Y, Li P, *et al.* Bandwidth-control orbital-selective delocalization of 4f electrons in epitaxial Ce films. *Nat Commun*, 2021, 12: 2520
- 40 Marin R, Jaque D. Doping lanthanide ions in colloidal semiconductor nanocrystals for brighter photoluminescence. *Chem Rev*, 2021, 121: 1425–1462
- 41 Dang P, Li G, Yun X, *et al.* Thermally stable and highly efficient red-emitting  $\text{Eu}^{3+}$ -doped  $\text{Cs}_3\text{GdGe}_3\text{O}_9$  phosphors for wleds: Non-concentration quenching and negative thermal expansion. *Light Sci Appl*, 2021, 10: 29
- 42 You W, Tu D, Zheng W, *et al.* Large-scale synthesis of uniform lanthanide-doped  $\text{NaREF}_4$  upconversion/downshifting nanoprobe for bioapplications. *Nanoscale*, 2018, 10: 11477–11484
- 43 Liu J, Pan L, Shang C, *et al.* A highly sensitive and selective nanosensor for near-infrared potassium imaging. *Sci Adv*, 2020, 6: eaax9757
- 44 Zhou B, Tang B, Zhang C, *et al.* Enhancing multiphoton upconversion through interfacial energy transfer in multilayered nanoparticles. *Nat Commun*, 2020, 11: 1174
- 45 Huang J, Li J, Zhang X, *et al.* Artificial atomic vacancies tailor near-infrared II excited multiplexing upconversion in core-shell lanthanide nanoparticles. *Nano Lett*, 2020, 20: 5236–5242
- 46 Zhang M, Zheng W, Liu Y, *et al.* A new class of blue-LED-excitable NIR-II luminescent nanoprobe based on lanthanide-doped  $\text{CaS}$  nanoparticles. *Angew Chem Int Ed*, 2019, 58: 9556–9560
- 47 Wang S, Zhang C, Zheng W, *et al.* A general strategy via charge transfer sensitization to achieve efficient NIR luminescence in lanthanide-doped  $\text{NaGdS}_2$  nanocrystals. *J Mater Chem C*, 2021, 9: 5148–5153
- 48 Jarý V, Havlák L, Bárta J, *et al.* Optical, structural and paramagnetic properties of Eu-doped ternary sulfides  $\text{ALnS}_2$  ( $\text{A} = \text{Na}, \text{K}, \text{Rb}; \text{Ln} = \text{La}, \text{Gd}, \text{Lu}, \text{Y}$ ). *Materials*, 2015, 8: 6978–6998
- 49 Zhang C, Zhang M, Zheng W, *et al.* A new class of luminescent nanoprobe based on main-group  $\text{Sb}^{3+}$  emitters. *Nano Res*, 2021, doi: 10.1007/s12274-021-3454-4
- 50 Gouget G, Pellerin M, Al Rahal Al Orabi R, *et al.* Rare-earth sulfide nanocrystals from wet colloidal synthesis: Tunable compositions, size-dependent light absorption, and sensitized rare-earth luminescence. *J Am Chem Soc*, 2021, 143: 3300–3305
- 51 Smet PF, Moreels I, Hens Z, *et al.* Luminescence in sulfides: A rich history and a bright future. *Materials*, 2010, 3: 2834–2883
- 52 Wang J, Zhu Y, Grimes CA, *et al.* Multicolor lanthanide-doped  $\text{CaS}$  and  $\text{SrS}$  near-infrared stimulated luminescent nanoparticles with bright emission: Application in broad-spectrum lighting, information coding, and bio-imaging. *Nanoscale*, 2019, 11: 12497–12501
- 53 Jia D, Wang X. Alkali earth sulfide phosphors doped with  $\text{Eu}^{2+}$  and  $\text{Ce}^{3+}$  for LEDs. *Optical Mater*, 2007, 30: 375–379
- 54 Huang P, Zheng W, Tu D, *et al.* Unraveling the electronic structures of neodymium in  $\text{LiLuF}_4$  nanocrystals for ratiometric temperature sensing. *Adv Sci*, 2019, 6: 1802282
- 55 Hazra C, Skripka A, Ribeiro SJL, *et al.* Erbium single-band nanothermometry in the third biological imaging window: Potential and limitations. *Adv Opt Mater*, 2020, 8: 2001178
- 56 Van Haecke JE, Smet PF, De Keyser K, *et al.* Single crystal  $\text{CaS}:\text{Eu}$  and  $\text{SrS}:\text{Eu}$  luminescent particles obtained by solvothermal synthesis. *J Electrochem Soc*, 2007, 154: J278–J282
- 57 Chen D, Yu Y, Huang F, *et al.* Modifying the size and shape of monodisperse bifunctional alkaline-earth fluoride nanocrystals through lanthanide doping. *J Am Chem Soc*, 2010, 132: 9976–9978
- 58 Raubach CW, Gouveia AF, de Santana YVB, *et al.* Towards controlled synthesis and better understanding of blue shift of the  $\text{CaS}$  crystals. *J Mater Chem C*, 2014, 2: 2743–2750
- 59 Hüttel B, Troppenz U, Velthaus KO, *et al.* Luminescence properties of  $\text{SrS}:\text{Ce}^{3+}$ . *J Appl Phys*, 1995, 78: 7282–7288
- 60 Zhao Y, Rabouw FT, van Puffelen T, *et al.* Lanthanide-doped  $\text{CaS}$  and  $\text{SrS}$  luminescent nanocrystals: A single-source precursor approach for doping. *J Am Chem Soc*, 2014, 136: 16533–16543
- 61 Miyakawa T, Dexter DL. Phonon sidebands, multiphonon relaxation of excited states, and phonon-assisted energy transfer between ions in solids. *Phys Rev B*, 1970, 1: 2961–2969
- 62 Salley GM, Valiente R, Güdel HU. Phonon-assisted cooperative sensitization of  $\text{Tb}^{3+}$  in  $\text{SrCl}_2:\text{Yb}, \text{Tb}$ . *J Phys-Condens Matter*, 2002, 14: 5461–5475
- 63 Ravotti F, Benoit D, Lefebvre P, *et al.* Time-resolved photoluminescence and optically stimulated luminescence measurements of picosecond-excited  $\text{SrS}:\text{Ce}, \text{Sm}$  phosphor. *J Appl Phys*, 2007, 102: 123102
- 64 Mei S, Zhou J, Sun HT, *et al.* Networking state of ytterbium ions probing the origin of luminescence quenching and activation in nanocrystals. *Adv Sci*, 2021, 8: 2003325
- 65 Zou Q, Huang P, Zheng W, *et al.* Cooperative and non-cooperative sensitization upconversion in lanthanide-doped  $\text{LiYbF}_4$  nanoparticles. *Nanoscale*, 2017, 9: 6521–6528
- 66 Shinn MD, Sibley WA, Drexhage MG, *et al.* Optical transitions of  $\text{Er}^{3+}$  ions in fluorozirconate glass. *Phys Rev B*, 1983, 27: 6635–6648
- 67 Maurice E, Monnom G, Dussardier B, *et al.* Erbium-doped silica fibers for intrinsic fiber-optic temperature sensors. *Appl Opt*, 1995, 34: 8019–8025



- 68 Wei J, Lian W, Zheng W, *et al.* Sub-10 nm lanthanide-doped SrFCl nanoprobe: Controlled synthesis, optical properties and bioimaging. *J Rare Earths*, 2019, 37: 691–698
- 69 Brites CDS, Xie X, Debasu ML, *et al.* Instantaneous ballistic velocity of suspended brownian nanocrystals measured by upconversion nanothermometry. *Nat Nanotech*, 2016, 11: 851–856
- 70 Bastos ARN, Brites CDS, Rojas-Gutierrez PA, *et al.* Thermal properties of lipid bilayers determined using upconversion nanothermometry. *Adv Funct Mater*, 2019, 29: 1905474
- 71 Cui Y, Song R, Yu J, *et al.* Dual-emitting MOF superset of dye composite for ratiometric temperature sensing. *Adv Mater*, 2015, 27: 1420–1425
- 72 Brites CDS, Balabhadra S, Carlos LD. Lanthanide-based thermometers: At the cutting-edge of luminescence thermometry. *Adv Opt Mater*, 2019, 7: 1801239
- 73 Zhao Y, Wang X, Zhang Y, *et al.* Optical temperature sensing of up-conversion luminescent materials: Fundamentals and progress. *J Alloys Compd*, 2020, 817: 152691

**Acknowledgements** This work was supported by the Science and Technology Cooperation Fund between Chinese and Australian Governments (2017YFE0132300), the National Natural Science Foundation of China (22135008, 12074379, 21875250 and 12004384), the Natural Science Foundation of Fujian Province (2020I0037 and 2021L3024), the Chinese Academy of Sciences/State Administration of Foreign Experts Affairs (CAS/SAFEA) International Partnership Program for Creative Research Teams, and Fujian Science & Technology Innovation Laboratory for Optoelectronic Information of China (2021ZR125).

**Author contributions** Wei J, Zheng W and Chen X conceived the projects, wrote the paper and were primarily responsible for the experiments. Wei J, Liu Y and Zhang M carried out the synthesis and characterization of the NCs. Wei J, Huang P, Gong Z and Li R measured the PL spectra and analyzed the data. All authors contributed to the general discussion.

**Conflict of interest** The authors declare that they have no conflict of interest.

**Supplementary information** Supplementary data are available in the online version of the paper.



**Jiaojiao Wei** earned her master's degree from Fujian Normal University (2018). She is currently a PhD student in inorganic chemistry at Fuzhou University. She joined Prof. Xueyuan Chen's group at Fujian Institute of Research on the Structure of Matter (FJIRSM), Chinese Academy of Sciences (CAS) in September 2016. Her research interest focuses on the controlled synthesis and optical spectroscopy of inorganic luminescent nanomaterials.



**Wei Zheng** was born in Fujian province of China. He earned his BSc degree (2007) in material forming and control engineering from Sichuan University and received his PhD degree (2012) in condensed matter physics from FJIRSM, CAS. He joined Prof. Xueyuan Chen's group in 2012 and was promoted to a professor in 2019. His research interest focuses on the controlled synthesis, optical properties and applications of inorganic luminescent nanomaterials, including lanthanide luminescent nanoparticles and perovskite nanocrystals.



**Xueyuan Chen** is editor-in-chief of *Journal of Luminescence*. He earned his BSc degree from the University of Science and Technology of China (1993) and his PhD degree from FJIRSM, CAS (1998). From 2001 to 2005, he was a postdoctoral research associate at the Chemistry Division of Argonne National Laboratory, U.S. Department of Energy, where he studied the photophysics and photochemistry of heavy elements. In 2005, he joined the faculty at FJIRSM, where he is currently a professor and group leader in materials chemistry and physics. His research focuses on the electronic structures, optical properties and applications of inorganic luminescent materials, such as lanthanide (rare-earth) nano-bioprobes and LED phosphors.

## 蓝光LED可激发的稀土掺杂SrS近红外二区纳米荧光探针及温度传感

委娇娇<sup>1,2</sup>, 刘友宇<sup>1,2</sup>, 张美然<sup>2</sup>, 郑伟<sup>1,2,3\*</sup>, 黄萍<sup>1,2,3</sup>, 宫仲亮<sup>2</sup>, 李仁富<sup>2,3</sup>, 陈学元<sup>1,2,3\*</sup>

**摘要** 稀土掺杂近红外二区纳米荧光探针在许多技术领域都具有广泛的应用前景,但目前受限于稀土离子的4f→4f禁戒跃迁导致材料的吸收强度弱、发光效率低。本文报道了一种基于SrS纳米晶Ce<sup>3+</sup>到Er<sup>3+</sup>和Nd<sup>3+</sup>高效能量传递的新型蓝光LED可激发的近红外二区纳米荧光探针。通过Ce<sup>3+</sup>的4f→5d吸收允许跃迁敏化,该纳米晶可实现Er<sup>3+</sup>和Nd<sup>3+</sup>的高效近红外二区发光,其荧光量子产率分别为2.9%和2.3%。利用Er<sup>3+</sup>的<sup>4</sup>I<sub>13/2</sub>热耦合晶体场子能级的近红外二区发光,该纳米晶可作为一种蓝光LED激发的近红外二区纳米荧光探针用于比率式温度传感。这些结果展示了SrS:Ln<sup>3+</sup>纳米晶在近红外二区波段的发光优点,为多功能稀土硫化物基纳米荧光探针的设计开发提供了新思路。